Journal of Materials Chemistry B

ROYAL SOCIETY OF CHEMISTRY

PAPER

View Article Online
View Journal | View Issue

Cite this: J. Mater. Chem. B, 2023, 11, 8649

Hydrogen-bonded organic framework-stabilized charge transfer cocrystals for NIR-II photothermal cancer therapy†

Jiakang Tang,[ab] Leihou Shao,[ab] Ji Liu,[ab] Qizhen Zheng,[ab] Xinyi Song,[c] Lanhua Yi *[c] and Ming Wang *[ab]

Received 29th June 2023,
Accepted 10th August 2023

DOI: 10.1039/d3tb01475d

rsc.li/materials-b

Charge-transfer (CT) cocrystals consisting of an electron donor and acceptor have gained attention for designing photothermal (PT) conversion materials with potential for biomedical and therapeutic use. However, the applicability of CT cocrystals is limited by their low stability and aqueous dispersity in biological settings. In this study, we present the self-assembly of CT cocrystals within hydrogen-bonded organic frameworks (HOFs), which not only allows for the dispersion and stabilization of cocrystals in aqueous solution but also promotes the CT interaction within the confined space of HOFs for photothermal conversion. We demonstrate that the CT interaction-driven self-assembly of tetrathiafulvalene (TTF) and tetracyanoquinodimethane (TCNQ) with PFC-1 HOFs results in the formation of cocrystal-encapsulated **TQC@PFC-1** while retaining the crystalline structure of the cocrystal and PFC-1. **TQC@PFC-1**, in particular, exhibits significant absorption in the second near-infrared region (NIR-II) and excellent photothermal conversion efficiency, as high as 32%. Cellular delivery studies show that **TQC@PFC-1** can be internalized in different types of cancer cells, leading to an effective NIR-II photothermal therapy effect both in cultured cells and *in vivo*. We anticipate that the strategy of self-assembly and stabilization of CT cocrystals in nanoscale HOFs opens the path for tuning their photophysical properties and interfacing cocrystals with biological settings for photothermal therapeutic applications.

Introduction

Organic charge-transfer (CT) cocrystals are a class of crystalline materials that self-assemble from an electron-rich donor and an electron-deficient acceptor *via* CT interactions.[1,2] The charge transfer occurring in CT cocrystals leads to intermolecular electron delocalization, which confers distinct magnetic and optical properties to cocrystals for use in molecular electronics,[3–7] nonlinear optics,[8–11] and ferroelectricity.[12,13] Moreover, nonradiative decay of photoexcited states in CT cocrystals can generate a photothermal (PT) effect[1,14,15] for use in PT imaging[16] and solar-thermal conversions.[17,18] In addition, the CT interaction in cocrystals can be tailored by selecting a suitable donor and acceptor, allowing for the tuning of their absorption to the near-infrared (NIR) region.[14,15] This feature is highly desired for biomedical use due to the low photo toxicity and excellent tissue penetration ability of NIR light.[19,20] However, the potential of CT cocrystals for biomedical and therapeutic use is greatly hindered by their low aqueous dispersity and stability in biological settings, which mainly arise from the intrinsic hydrophobic nature and supramolecular interactions of cocrystals.[21] Recently, efforts have been made to overcome these limitations, such as growing co-crystals on the surface of bioactive glass scaffolds[22] or encapsulating cocrystals into metal–organic frameworks (MOFs)[23] to interface cocrystals with biological settings. Despite these efforts, aqueous-dispersible CT cocrystals with tunable NIR absorption, especially in the second NIR region (NIR-II, 1000–1700 nm) for PT conversion, are still deficient, limiting the full realization of their biomedical potential.

Compared to MOFs[24,25] and covalent organic frameworks[26,27] which are connected by coordination or covalent bonding, hydrogen-bonded organic frameworks (HOFs) are porous nanomaterials that are held together by intermolecular hydrogen bonding of strategically pre-designed molecular subcomponents.[28–30] The porous structure of HOFs has been harnessed to integrate functional moieties for diverse applications,[31–34] such as heterogeneous catalysis,[35] ion conduction[36] and gas separation.[37] Furthermore,

[a] Beijing National Laboratory for Molecular Sciences, CAS Key Laboratory of Analytical Chemistry for Living Biosystems, Institute of Chemistry, Chinese Academy of Sciences, Beijing 100190, China. E-mail: mingwang@iccas.ac.cn
[b] University of Chinese Academy of Sciences, Beijing 100049, China
[c] Key Laboratory of Environmentally Friendly Chemistry and Applications of Ministry of Education, School of Chemistry, Xiangtan University, Xiangtan 411105, P. R. China. E-mail: yilanhua@xtu.edu.cn

† Electronic supplementary information (ESI) available. See DOI: https://doi.org/10.1039/d3tb01475d

compared to MOFs, the dynamic and metal-free nature of hydrogen bonding endows HOFs with mild synthesis in aqueous solution and high biocompatibility. These properties have facilitated the biomedical use of HOFs for drug delivery[38] and antimicrobial therapy.[39,40] For example, the incorporation of protein[41–45] into nanoscale HOFs has enabled intracellular protein delivery for molecular catalysis in living cells.[46] Encapsulating neural stem cells into HOFs provides a promising approach for developing new treatments for neurodegenerative disease.[47,48] We envision that using HOFs as a host to encapsulate CT cocrystals will not only disperse and stabilize cocrystals in an aqueous solution but also allow the control of CT interaction within the constrained space of HOFs for achieving tunable photophysical properties, thus maximizing their biomedical applications.

Herein, we report the self-assembly of CT cocrystals within nanoscale HOFs, which can induce PT conversion in the NIR-II region for photothermal cancer therapy. Our approach involves the hydrogen bonding-driven self-assembly of 1,3,6,8-tetrakis-(benzoic acid)pyrene (H_4TBAPy), a precursor for PFC-1 HOFs which shows high stability against acid conditions and various solvents,[33] with different electron donor–acceptor pairs to form CT cocrystal-encapsulated HOFs (Scheme 1). By selecting electron donors and acceptors with appropriate HOMO–LUMO (highest occupied/lowest unoccupied molecular orbital) bandgaps, we can tune the absorption of the cocrystal-encapsulated HOFs to the NIR-II region. Especially, we demonstrate that the *in situ* self-assembly of tetrathiafulvalene (**TTF**) as the electron donor and tetracyanoquinodimethane (**TCNQ**) as the electron acceptor, along with H_4TBAPy, forms the cocrystal-encapsulated HOF, **TQC@PFC-1**. Cryo-transmission electron microscopy (Cryo-TEM) characterization of **TQC@PFC-1** shows that the cocrystals and HOFs maintain their crystalline structure and skeleton, respectively. The CT interaction between TTF and TCNQ results in a broad absorption of **TQC@PFC-1** in the NIR-II region for an excellent PT conversion with efficiency as high as 32%, which is one of the most efficient cocrystal-based PT conversions, particularly in the NIR-II region.[16–18,22,23] Furthermore, our cellular delivery study shows that **TQC@PFC-1** can efficiently enter cells, demonstrating a PTT effect to ablate tumor cell growth under the irradiation of NIR-II light in both cultured cells and a tumor-bearing mouse xenograft. Our study highlights the potential of self-assembly and stabilization of CT cocrystals in nanoscale HOFs to tune their photophysical properties and interface cocrystals with biological settings for therapeutic applications.

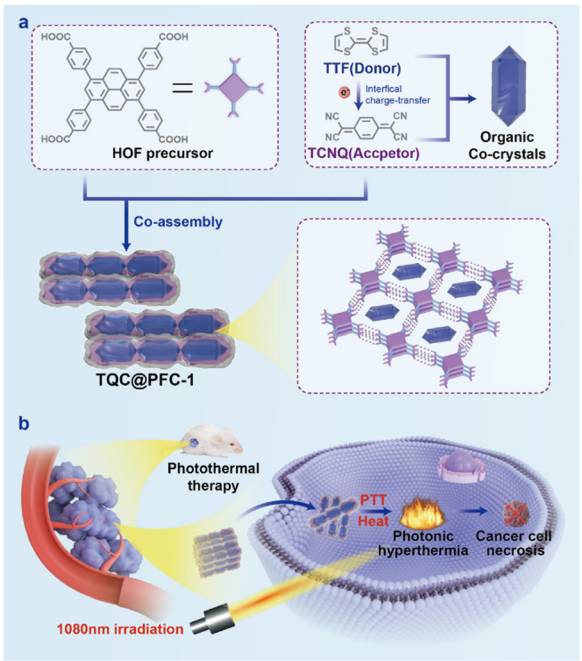

Scheme 1 (a) Schematic illustration of *in situ* assembly of an organic CT co-crystal, **TQC** within hydrogen-bonded organic frameworks (HOFs), **PFC-1**; and (b) photothermal study of **TQC@PFC-1** for cancer therapy.

Results and discussion

Synthesis and characterization of cocrystal@HOFs

As shown in Scheme 1, we employed a co-assembly strategy to prepare and encapsulate CT cocrystals into PFC-1 HOFs. To prepare TQC-encapsulate PFC-1 HOFs, TTF and TCNQ in an equal molar ratio (Fig. S1, ESI†) were first dissolved in DMF, followed by addition of the PFC-1 precursor, H_4TBAPy, and transfer of the mixture to an aqueous solution. To prepare HOFs that encapsulate various CT cocrystals, TTF was combined with 1,2,4,5-tetracyanobenzene (TCNB) to create **TBC**, while dibenzotetrathiafulvalene (DBTTF) was mixed with TCNB to form **DTC**. To demonstrate the advantage of HOF encapsulation for stabilizing and dispersing CT cocrystals in aqueous solutions, we prepared co-crystals without HOF encapsulation by directly mixing the subcomponents in acetonitrile or tetrahydrofuran (THF).[16,17] Morphology characterization of the cocrystals using scanning electron microscopy (SEM) (Fig. S2 and S3, ESI†) reveals that all CT cocrystals formed large particles with sizes greater than 5 μm. In contrast, cocrystal-encapsulated PFC-1 exhibits a nanorod morphology similar to that of PFC-1, with decreased nanoparticle size down to ~300–400 nm in diameter (Fig. 1a and Fig. S3, ESI†). Furthermore, the powder X-ray diffraction (PXRD) pattern of all three cocrystals before and after PFC-1 encapsulation (Fig. 1b and Fig. S4, ESI†) showed similar characteristic peaks, indicating the retention of the cocrystal structure within HOFs. In addition, the preservation of characteristic PXRD patterns attributed to HOFs in the three cocrystals@PFC-1 confirmed the integrity of PFC-1 during the co-assembly.

The solid-state absorption spectra of all cocrystals@PFC-1 show a broad peak over 800 nm, which is significantly redshifted compared to that of H_4TBAPy or the donor/acceptor subcomponents (Fig. 1c and Fig. S5, ESI†). This finding indicates a highly efficient charge-transfer interaction between the donors and acceptors after HOF encapsulation. Moreover, we found that selecting electron donor–acceptor pairs with an appropriate HOMO–LUMO bandgap allows the assembly of cocrystals that exhibits varied and controllable absorption (Fig. S5, ESI†). In this

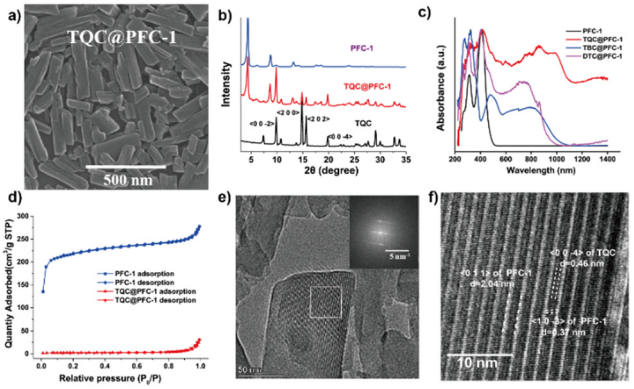

Fig. 1 Characterization of **TQC@PFC-1**. (a) SEM image of **TQC@PFC-1**. (b) PXRD spectra of TQC, PFC-1 and **TQC@PFC-1**. (c) Solid-state UV/Vis absorption spectra of PFC-1, **TQC@PFC-1**, **TBC@PFC-1** and **DTC@PFC-1**. (d) N_2 uptake isotherms of PFC-1 and **TQC@PFC-1**. (e) Structural profile of **TQC@PFC-1** characterized by cryo-TEM and the fast Fourier transform (FFT) pattern of the selected area (inset). (f) The amplified cryo-TEM image of the selected area highlighted in the white frame in (e).

study, we focused on cocrystals **DTC**, **TBC**, and **TQC**, which have small HOMO–LUMO energy bandgaps (1.43, 1.3, and 0.44 eV respectively) predicted by density functional theory (DFT) calculations[15] (Fig. S1, ESI†). Therefore, the small HOMO–LUMO bandgaps of cocrystals bestow them with a preferred non-radiative electron decay and redshifted light absorption range,[1,15] which agrees well with the measured absorption spectra of cocrystals-encapsulated PFC-1(Fig. 1c). Notably, **TQC@PFC-1** displays strong absorption in the UV to NIR range (300–1400 nm), even reaching the NIR-II region.

Given the high desirability of **TQC@PFC-1** for biomedical applications due to its absorption in the NIR-II region, we subsequently focused on the comprehensive study and characterization of **TQC@PFC-1**. We began by validating the CT interaction between TTF and TCNQ through FT-IR and Raman spectroscopic analyses of **TQC@PFC-1**. The FT-IR spectrum of TCNQ exhibited a redshift of the C≡N stretching vibration from ~2219 cm^{-1} to ~2188 cm^{-1} in **TQC@PFC-1**, indicative of the increased electron density of the conjugated planar structure of TCNQ as a result of the CT interaction (Fig. S6, ESI†). Similarly, the Raman spectrum of **TQC@PFC-1** (Fig. S7, ESI†) showed a downfield shift of the –C=CH bending band attributed to TCNQ from ~1205 cm^{-1} to ~1198 cm^{-1} in **TQC@PFC-1**, signifying the electron delocalization from TTF to TCNQ. In addition, we conducted the XPS measurements of **TQC@PFC-1**. The XPS characterization revealed a clear increase in the binding energy of the N 1s peak and decrease in the binding energy of the S 2p1 and S 2p3 peaks, compared to TCNQ and TTF, respectively. These results provide strong evidence of the intermolecular charge–transfer interaction between TCNQ and TTF within **TQC@PFC-1** (Fig. S8, ESI†). Besides, thermogravimetric analysis (TGA) revealed that **TQC@PFC-1**, unlike PFC-1, started to undergo thermal decomposition at ~200 °C, similar to **TQC** (Fig. S9, ESI†). Additionally, the nitrogen gas uptake study showed that the encapsulation of **TQC** into PFC-1 significantly reduced the inner surface area of PFC-1 (Fig. 1d). This effect may be attributed to the occupation of the inner pore of PFC-1 by **TQC**. Furthermore, the EDX mapping of **TQC@PFC-1** confirmed the homogeneous distribution of **TQC** within PFC-1 (Fig. S10, ESI†). The fluorescence spectra revealed that PFC-1 and **TQC@PFC-1** exhibited a similar emission peak at approximately 370 nm when excited at 320 nm (Fig. S11, ESI†). Additionally, the stability study demonstrated that **TQC@PFC-1** could remain well-dispersed in water for several hours, whereas **TQC** would precipitate within minutes. Moreover, both **TQC** and **TQC@PFC-1** exhibited good stability when treated with acetone, methanol, or hydrochloric acid (Fig. S12, ESI†).

The microstructure of **TQC@PFC-1** was further characterized using cryo-transmission electron microscopy (cryo-TEM). In the cryo-TEM images of TQC and PFC-1, lattice planes along the $\langle 0\,0\,-4\rangle$ direction of TQC and $\langle 1\,0\,-3\rangle$ and $\langle 0\,1\,1\rangle$ directions of PFC-1 were observed, respectively, as shown in Fig. S13 (ESI†). These lattice planes were also observed in the cryo-TEM image of **TQC@PFC-1** (Fig. 1e and f), indicating the preservation of the crystalline structure of both PFC-1 and TQC in **TQC@PFC-1**. Importantly, the lattice plane corresponding to TQC was observed to be intercalated within the ordered 1D channel-like pores (~2 nm) of PFC-1, providing evidence for the successful encapsulation of TQC into HOFs. Therefore, cryo-TEM imaging confirmed the localization of TQC in the ordered one-dimensional channel-like pores of PFC-1, which supported the preservation of the lattice structures of TQC and PFC-1 during the co-assembly process. This observation was consistent with the PXRD characterization of **TQC@PFC-1** (Fig. 1b).

Photothermal effect of TQC@PFC-1

The photothermal conversion of **TQC@PFC-1** in the NIR-II region was studied. Dynamic light scattering (DLS) measurements of the aqueous **TQC@PFC-1** solution indicate good water dispersity with a nanoparticle size of around 250 nm in diameter (Table S1 and Fig. S14, ESI†). The increased zeta potential of **TQC@PFC-1** might be owing to the enhanced hydrophobicity of PFC-1 when loaded with TQC. Meanwhile, the **TQC@PFC-1** solution (1 mg mL^{-1}) shows broad absorption in the range of 500–1100 nm (Fig. S15, ESI†), indicating that the dispersion of **TQC@PFC-1** in aqueous solution has minimal effect on the CT interaction between TTF and TCNQ. **TQC@PFC-1** shows a distinct photothermal effect in the presence of light irradiation. As shown in Fig. 2a, the temperature of the aqueous **TQC@PFC-1** solution (1 mg mL^{-1}) increased up to 60-fold compared to that of PFC-1 ($\Delta T \approx 36$ °C *vs.* $\Delta T \approx 0.5$ °C) when both solutions were irradiated with NIR-II light (1080 nm, 5 min, 1.5 W cm^{-2}). Additionally, the photothermal conversion of **TQC@PFC-1** depended on its concentration and the laser power applied to the solution. Increasing the concentration of **TQC@PFC-1** or the laser power both led to an increase in solution temperature (Fig. 2b and c). The PT conversion efficiency of **TQC@PFC-1** was calculated to be 32.0%, following reported methods[16,23] (Fig. S16, ESI†), representing one of the most efficient cocrystal-based PT conversions, particularly in the NIR-II region.[16,22,23] Furthermore, the **TQC@PFC-1** solution showed a 1.4-fold higher temperature increment than that of **TQC** or physical mixture of **TQC** and PFC-1 under the same concentration and irradiation time (Fig. S17, ESI†), suggesting

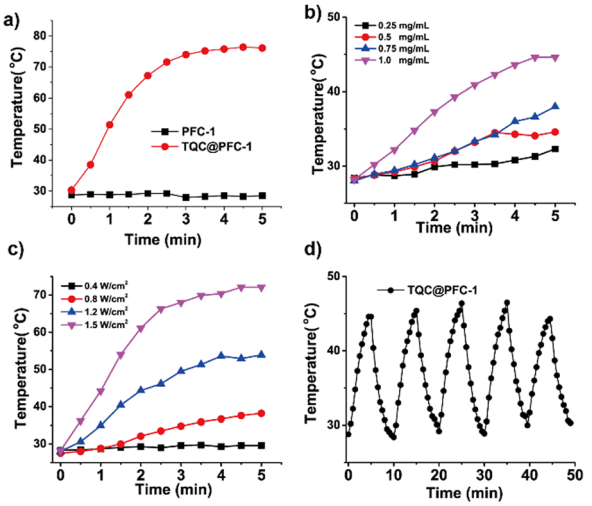

Fig. 2 Photothermal study of aqueous **TQC@PFC-1** solution. (a) Comparison of the photothermal effect of PFC-1 and **TQC@PFC-1** dispersed in aqueous solution (1 mg mL^{-1}) under 1080 nm laser irradiation (1.5 W cm^{-2}). (b) Photothermal conversion of **TQC@PFC-1** with different concentrations (0.25–1 mg mL^{-1}) under 1080 nm laser irradiation (0.8 W cm^{-2}). (c) Photothermal conversion of **TQC@PFC-1** aqueous solution (1 mg mL^{-1}) under 1080 nm laser irradiation with different exposure intensities (0.4–1.5 W cm^{-2}). (d) Photothermal stability study of **TQC@PFC-1** in aqueous solution (1 mg mL^{-1}, 1080 nm, 0.8 W cm^{-2}) during five cycles of heating–cooling processes.

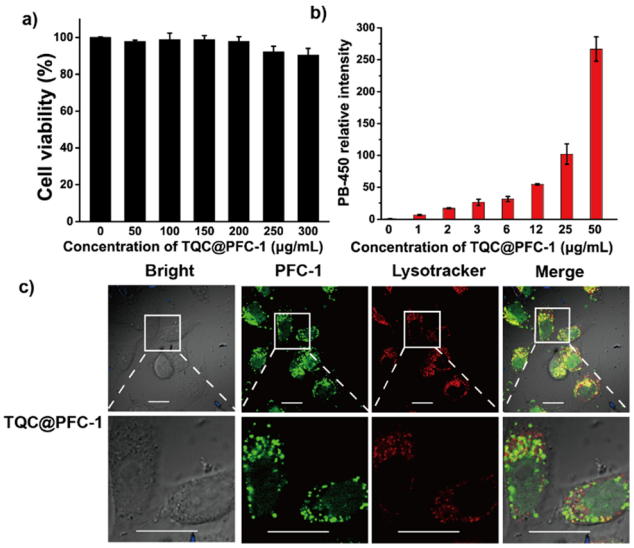

Fig. 3 (a) Cytotoxicity study of **TQC@PFC-1** against HeLa cells. The cells were treated with **TQC@PFC-1** at indicated concentrations for 18 h, followed by cell viability measurements using MTT assay. (b) Cellular uptake study of **TQC@PFC-1** by treating HeLa cells with different concentrations of HOFs for 18 h, followed by flow cytometry analysis to quantify relative fluorescence intensity of **TQC@PFC-1**-treated cells compared to that of untreated cells. The fluorescent intensity was normalized to cells without TQC@PFC-1 treatment. The data were presented as mean ± SD (n = 3). (c) CLSM images of HeLa cells incubated with 0.1 mg mL^{-1} **TQC@PFC-1** for 18 h. The endosome/lysosome was stained by 100 nM LysoTracker@Red before CSLM imaging. Scale bar: 20 μm.

an enhancement of the CT interaction between TTF and TCNQ within **TQC@PFC-1**, which may be attributed to the increased electron density in the cocrystals induced by the electron-rich framework of PFC-1. Moreover, **TQC@PFC-1** exhibited high photostability, as evidenced by the minimal decrease in the photothermal effect of **TQC@PFC-1** after multiple cycles of light irradiation (Fig. 2d).

Photothermal therapy study of TQC@PFC-1

We next sought to study the potency of **TQC@PFC-1** for photothermal therapy (PTT) for ablating cancer cells. Firstly, we evaluated the stability of **TQC@PFC-1** in cell culture medium and confirmed its stability through a minimal change in the PXRD pattern of **TQC@PFC-1** before and after 24 h of incubation with Dulbecco's modified Eagle's medium (DMEM) for 24 h (Fig. S18, ESI†). We then studied the cytotoxicity of **TQC@PFC-1** against cancerous HeLa cells (Fig. 3a). The results showed low cytotoxicity at the indicated concentrations to prohibit HeLa cell growth, indicating excellent biocompatibility of **TQC@PFC-1** for PTT. To determine the delivery efficiency, we performed a detailed cellular uptake study by treating HeLa cells with different concentrations of **TQC@PFC-1**, followed by flow cytometry analysis. We found that **TQC@PFC-1** (12 μg mL^{-1}) was delivered to over 95% of HeLa cells after 18 hours of incubation, and the cellular fluorescence intensity increased up to 50-fold compared to that of untreated cells, confirming efficient delivery of **TQC@PFC-1** to HeLa cells (Fig. 3b and Fig. S19, 20, ESI†). Furthermore, we investigated the intracellular trafficking of **TQC@PFC-1** by pre-treating HeLa cells with **TQC@PFC-1** (0.1 mg mL^{-1}), followed by endo/lysosome staining using LysoTracker@Red (Fig. 3c). Confocal laser scanning microscopy (CLSM) imaging indicated the internalization of TQC@PFC-1 by HeLa cells and efficient endosome escape of TQC@PFC-1 after entering cells, with a calculated colocalization coefficient (Pearson's correlation coefficient) of approximately 0.41. In addition, confocal laser scanning microscopy (CLSM) images of cells incubated with **TQC@PFC-1** at various time points further confirmed efficient endosome escape after 3 hours of incubation (Fig. S21, ESI†).

The effectiveness of **TQC@PFC-1** for photothermal therapy (PTT) was investigated using a Calcein AM/PI co-staining assay. Treatment with either **TQC@PFC-1** (0.2 mg mL^{-1}) or laser irradiation (1080 nm, 1.5 W cm^{-2}) alone did not show any significant cytotoxic effects on HeLa cells. However, the combination of **TQC@PFC-1** and NIR-II laser irradiation led to significant cell necrosis (Fig. 4a), demonstrating the synergistic effect of **TQC@PFC-1** treatment and NIR-II laser irradiation for PTT. Viability assays of HeLa cells receiving different treatments indicated that neither **TQC@PFC-1** incubation (0.2 mg mL^{-1}) nor laser irradiation (1080 nm, 1.5 W cm^{-2}) caused significant cell death (Fig. 4b). However, the treatment of **TQC@PFC-1** followed by NIR-II laser irradiation reduced cell viability to approximately 36% of non-treated controls. Additionally, the PTT and antitumor effect of **TQC@PFC-1** depended on its concentration added to the cells (Fig. 4c). The cell viability was decreased to 30% when the concentration of **TQC@PFC-1** was increased from 0.05 to 0.25 mg mL^{-1}. Furthermore, the cell death pathway was explored using Annexin V-FITC/PI staining assay.

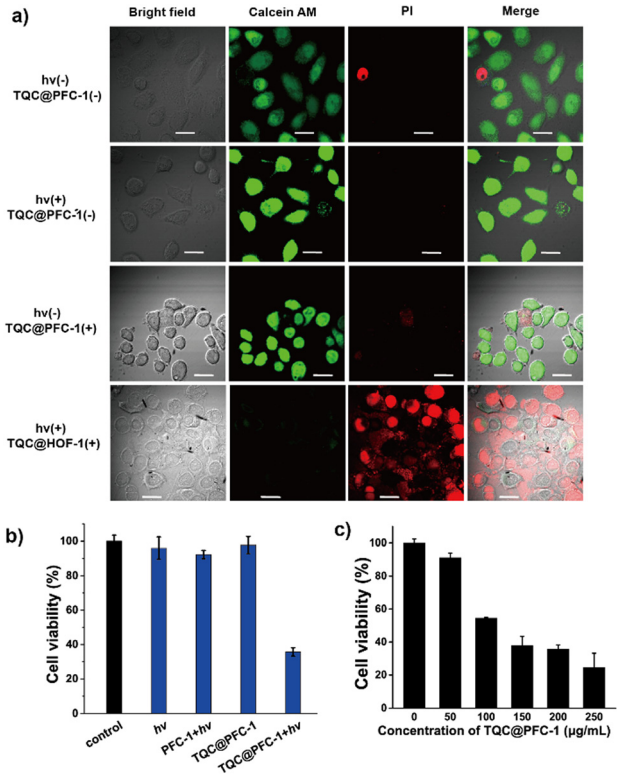

Fig. 4 (a) Calcein AM (green) and propidium iodide (red) co-staining imaging of HeLa cells after different treatments. Cells were incubated with **TQC@PFC-1** solution (0.25 mg mL^{-1}) for 2 h before laser irradiation. The treated cells were incubated for 18 h before co-staining using Calcein AM/PI Living/Dead cell double staining kit. *hv* represents NIR laser irradiation (1080 nm, 1.5 W cm^{-2}, 5 min). Scale bar: 20 μm. (b) Viability of HeLa cells treated with 0.2 mg mL^{-1} PFC-1 or 0.2 mg mL^{-1} **TQC@PFC-1** for 2 h followed by light irradiation (1080 nm, 1.5 W cm^{-2}) for 5 min, the treated cells were incubated for another 18 h before the measurement of viability using an MTT assay. (c) Viability of HeLa cells incubated with **TQC@PFC-1** at different concentrations with the same treatments as described above. The data were presented as mean ± SD (n = 3).

The results showed that cells treated with **TQC@PFC-1** followed by NIR-II laser irradiation exhibited significant cell necrosis (47%), which could be attributed to the photothermal effect (Fig. S22, ESI†). Importantly, we found that the PTT effect of **TQC@PFC-1** was not specific to different types of cancer cells. The treatment of either B16-F10 murine melanoma cells or 4T1 breast cancer cells with different concentrations of **TQC@PFC-1**, followed by light irradiation showed similar cell growth prohibition effects to those observed with HeLa cells (Fig. S23 and S24, ESI†).

In vivo antitumor study of TQC@PFC-1

We evaluated the *in vivo* antitumor efficacy of **TQC@PFC-1** through a tumor-bearing mouse xenograft. A HeLa tumor-bearing mouse was injected with either phosphate buffer solution (PBS) as a negative control or **TQC@PFC-1**, followed by NIR-II laser irradiation. We evaluated the *in vivo* photothermal therapy (PTT) effect and antitumor efficacy by comparing the tumor growth suppression effect. As depicted in Fig. 5a, the monitoring of tumor growth following different treatments indicates that neither laser

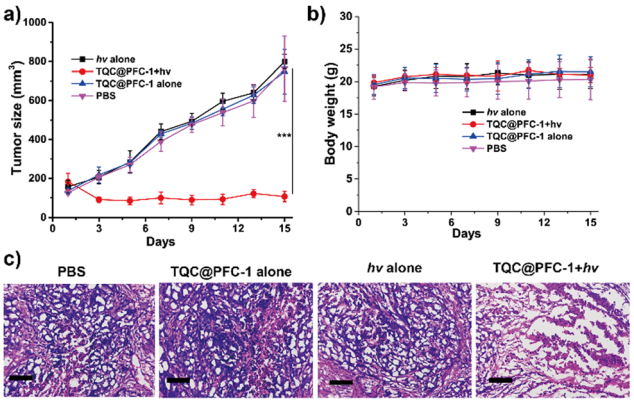

Fig. 5 (a) Tumor growth curves of HeLa tumor-bearing mice received different treatments as indicated. (b) Body weight change of HeLa tumor-bearing mice after different treatments. (c) H & E analysis of tumor tissues collected from mice received different treatments as indicated. Scale bar 200 μm. The data were presented as mean ± SD (n = 5). *** represents $p < 0.001$.

irradiation (1080 nm, 0.9 W cm^{-2}, 6 min) nor **TQC@PFC-1** (4.2 mg kg^{-1}) alone exhibited an apparent tumor growth suppression effect compared to that of PBS injections. In contrast, **TQC@PFC-1** administration followed by laser irradiation suppressed tumor growth by up to 90% (Fig. S25, ESI†). Histological hematoxylin and eosin (H & E) staining of tumor tissues of mice that received PBS or **TQC@PFC-1** injections exhibited obvious necrotic areas in **TQC@PFC-1** treatment followed by laser irradiation (Fig. 5c), confirming the effectiveness of **TQC@PFC-1** for *in vivo* photothermal cancer therapy. We monitored the weight of mice in all four groups and observed minimal change, indicating a negligible negative effect of **TQC@PFC-1** injections or laser irradiation on mouse health (Fig. 5b). Additionally, H & E analysis of the major organs (heart, liver, spleen, lungs, and kidneys) from mice that received the above treatments at the end of the study suggested minimal pathological tissue damage, indicating the high biocompatibility of **TQC@PFC-1** for antitumor study (Fig. S26, ESI†). Lastly, liver function analysis (Fig. S27, ESI†) further indicated the biocompatibility and minimal effect of **TQC@PFC-1** on mouse health.

Conclusions

In conclusion, we report the encapsulation and stabilization of organic CT cocrystals in nanoscale HOFs for photothermal conversion and cancer therapy. We demonstrate that by selecting an appropriate electron donor–acceptor pair for assembling CT cocrystals, we can tune the absorption of cocrystal@HOFs to the NIR-II region for photothermal therapy in both cultured cells and *in vivo*. Due to the strong CT interaction between TTF and TCNQ in HOFs, the rationally designed **TQC@PFC-1** exhibits a PT conversion efficiency as high as 32%, which represents one of the most efficient cocrystal-based PT conversions, particularly in the NIR-II region. We believe that the strategy of self-assembly and stabilization of CT cocrystals in nanoscale HOFs paves the way for tuning their photophysical properties

and interfacing cocrystals with biological settings for therapeutic promise.

Experimental section

General

1,3,6,8-Tetrakis(benzoic acid)pyrene (H_4TBAPy) was purchased from Yanshen Technology Co., Ltd (Jilin, China); tetrathiafulvalene (TTF) was purchased from Alfa Aesar (Heysham, England); dibenzotetrathiafulvalene (DBTTF) was purchased from Innochem (Beijing, China); 1,2,4,5-tetracyanobenzene (TCNB) was purchased from Ark Pharm (Chicago, USA); LysoTracker Red DND-99 for endosome staining was purchased from Beyotime (Shanghai, China); tetracyanoquinodimethane (TCNQ) and 3-(4,5-dimethylthiazol-2-yl)-2,5-diphenyltetrazolium bromide (MTT) were purchased from Aladdin (Shanghai, China). A calcein-AM/PI Living/Dead cell double staining kit was purchased from Solarbio (Beijing, China).

General characterization

Ultraviolet-visible (UV-Vis) spectra were recorded on a Lambda 1050+ spectrophotometer (PerkinElmer, USA). Fourier transform infrared (FT-IR) spectra were measured on the TENSOR-27 spectrometer (Bruker, Swiss). Nitrogen gas adsorption/desorption isothermal curves were recorded at 77 K up to 1 bar on ASAP 2020 surface area/pore size analyzer (Micromeritics, USA). Thermogravimetric analysis (TGA) was performed on TGA8000 (PerkinElmer, USA). X-Ray photoelectron spectroscopy (XPS) measurements were performed using an AXIS SUPRA+ X-ray photoelectron spectrometer equipped with a Mg Ka radiation source. Scanning electron microscopy (SEM) was performed on a Hitachi SU8020 electron microscope (Hitachi, Japan) at an accelerating voltage of 150 kV. Elemental analysis was carried out on a Thermo Flash Smart organic elemental analyzer (Thermo Scientific, USA). Zeta potential and dynamic light scattering (DLS) analysis were obtained on a Zetasizer Nano ZS ZEN3600 (Malvern, UK). Powder X-ray diffraction spectroscopy (PXRD) was performed using an Empyrean X-ray diffractometer (PANalytical, Holland). Cryo-transmission electron microscopy (Cryo-TEM) was performed using a Themis300 transmission electron microscope (Thermo Scientific, USA). To prevent structural damage by the electron beam during cryo-EM characterization of HOFs, the electron dose rate was set at approximately 4.5 electrons per pixel, and the total dose rate was approximately 6 electrons per $Å^2$ for each micrograph. The Raman experiments were conducted on a HORIBA LabRAM HR Evolution laser microscopic confocal Raman spectrometer (HORIBA, France). Confocal laser scanning microscopy (CLSM) experiments were conducted on an OLYMPUS FV1000-IX81 instrument (Olympus, Japan). The flow cytometric experiments were carried out with a CytoFLEX flow cytometry system (Beckman Coulter, USA).

Synthesis of PFC-1

PFC-1 was synthesized according to a reported method.[38] Briefly, H_4TBAPy (10 mg, 0.015 mmol) was first dissolved in 1.5 mL of DMF, the solution was then added with 10 mL water, followed by another 2 h of stirring. The resulted precipitate was purified by centrifugation at 15 000 rpm for 15 min, washed with water and ethanol twice before characterization or further use.

Synthesis of organic cocrystals

The CT cocrystals were prepared following previous reports.[16,17] In a typical procedure for the synthesis of TQC, a solution of TTF (20 mg, 94.9 μmol) dissolved in tetrahydrofuran (THF) was added dropwise to a solution of TCNQ (19.4 mg, 94.9 μmol) in THF. The cocrystals TQC were obtained by slow evaporation of THF. Similarly, TBC was prepared *via* the self-assembly of TTF (20 mg, 94.9 μmol) with TCNB (16.9 mg, 94.9 μmol) in THF, DTC was self-assembled from DBTTF (28.8 mg, 94.9 μmol) and TCNB (16.9 mg, 94.9 μmol) in acetonitrile.

Synthesis of TQC@PFC-1, TBC@PFC-1 and DTC@PFC-1

To synthesize PFC-1-encapsulated cocrystals, for instance, **TQC@PFC-1**, H_4TBAPy (10 mg, 0.015 mmol), TTF (3.1 mg, 0.015 mmol) and TCNQ (3.1 mg, 0.015 mmol) were dissolved in 1.5 mL of DMF, to the mixture was added with 10 mL water. The resulting mixture was stirred at room temperature for 3 h in the dark. **TQC@PFC-1** was isolated by centrifugation at 15 000 rpm for 15 min, then redispersed in water and sonicated for 10 minutes. Afterwards, the sample was isolated again by centrifugation. The resulting precipitate was washed twice with water and ethanol before vacuum drying. Elemental analysis of **TQC@PFC-1**: 4.41% N, 66.7% C, 3.86% H, 10.95% S and 14.1% O. Hence, by conversion, the molar ratio of H_4TBAPy, TTF, and TCNQ in the **TQC@PFC-1** complex was calculated to be 1.2/1/1. Similarly, **TBC@PFC-1** was self-assembled using H_4TBAPy (10 mg, 0.015 mmol), TTF (3.1 mg, 0.015 mmol), and TCNB (2.7 mg, 0.015 mmol). **DTC@PFC-1** was self-assembled using H_4TBAPy (10 mg, 0.015 mmol), DBTTF (4.6 mg 0.015 mmol), and TCNB (2.7 mg 0.015 mmol).

Photothermal effect characterization of TQC@PFC-1

To evaluate the photothermal effect of **TQC@PFC-1**, an aqueous solution of **TQC@PFC-1** at different concentrations was irradiated with 1080 nm light at the indicated power for 5 min. Next, the solution was cooled down to room temperature. The temperature of the solution was recorded using FLIR thermal camera at time intervals of 30 s.

Cell culture

All cells used in this study, including HeLa, 4T1, and B16F10 cells were purchased from the Natural Infrastructure of Cell Line (Beijing, China), and cultured in Dulbecco's modified Eagle's medium (DMEM) supplemented with 10% fetal bovine serum (FBS) and 1% penicillin/streptomycin at 37 °C in the presence of 5% CO_2.

Cellular uptake study of TQC@PFC-1

For the cellular uptake study of **TQC@PFC-1**, HeLa cells were seeded at a density of 1.5×10^4 cells in a glass bottom cell culture dish 24 h prior to experiment. At the day of study, the cells were incubated with **TQC@PFC-1** (0.1 mg mL^{-1}) for 18 h at

37 °C. Next, the cells were washed with 0.1% heparin solution twice and incubated with LysoTracker Red DND-99 (100 nM) for 15 min at 37 °C. Then, the cells were washed twice with Dulbecco's phosphate-buffered saline (DPBS) and imaged using CLSM. To further quantify the uptake efficiency, HeLa cells were seeded at a density of 2.5×10^4 cells per well in 48 well plates 24 h prior to the experiment. Then, cells were incubated with different concentrations of **TQC@PFC-1** for 18 h. At the end of incubation, the cells were washed with DPBS twice and harvested for flow cytometry analysis.

Photothermal therapy study of TQC@PFC-1

The biocompatibility and PTT effect of **TQC@PFC-1** were evaluated by treating HeLa cells with different concentrations of **TQC@PFC-1** and light irradiation, followed by a standard MTT assay to quantify the change of cell viability. Briefly, HeLa cells were seeded in a 96-well plate 24 h before the delivery experiment. At the day of experiment, the cells were treated with increased concentrations of **TQC@PFC-1**, followed by 5 min of light irradiation (1080 nm, 1.5 W cm^{-2}) 2 h post-delivery. Meanwhile, the treatments of **TQC@PFC-1** without light irradiation or light irradiation of cells alone were similarly performed as negative controls. The cells were washed with DPBS, incubated for another 18 h with fresh cell medium, washed with DPBS twice before cell viability measurements using an MTT assay. To demonstrate the general use of **TQC@PFC-1** for PTT, 4T1 cells or B16F10 cells were similarly treated with **TQC@PFC-1** as described above.

Calcein-AM/PI assay and Annexin V-FITC/PI assay of the PTT effect of TQC@PFC-1

Calcein-AM/PI Living/Dead staining and Annexin V-FITC/PI staining were used to further characterize the PTT effect of **TQC@PFC-1**. To this end, HeLa cells were seeded at a density of 1.5×10^4 cells in glass-bottom cell culture dish 24 h prior to the study. At the day of experiment, the cells were treated with **TQC@PFC-1** (diluted to 0.25 mg mL^{-1} in cell culture media) followed by 5 min of light irradiation (1080 nm, 1.5 W cm^{-2}) 2 h post delivery. Meanwhile, the treatments of **TQC@PFC-1** without light irradiation or light irradiation of cells alone were similarly performed as negative controls. Subsequently, the cells were incubated with refreshed cell culture medium for 18 h before Calcein AM/PI Living/Dead staining or Annexin V-FITC/PI staining according to the manufacturer's instruction and CLSM imaging.

Photothermal therapy study of TQC@PFC-1 *in vivo*

The animal experiments were performed with the approval of the Institutional Animal Care and Use Committee of the National Center for Nanoscience and Technology, China. To evaluate the PTT effect of **TQC@PFC-1** *in vivo*, a HeLa-tumor bearing mouse xenograft was generated by subcutaneously injecting HeLa cells (4×10^6 cells) to the right back region of four-week-old female BALB/c nude mice (purchased from Beijing Vital River Laboratory Animal Technology Co., Ltd). The tumor volume was calculated using a Vernier caliper using the equation: $A = \frac{a \times b^2}{2}$,[49] where A was the volume of tumor, a and b are the length and width of the tumor respectively. When the mouse tumor volume reached about 120 mm^3, the mice were subjected to four different treatments (n = 5 in each group): (1) PBS (70 μL); (2) **TQC@PFC-1** (1.3 mg mL^{-1}, 70 μL, ~4.2 mg kg^{-1}) alone; (3) PBS (70 μL) + *hv*; (4) **TQC@PFC-1** (1.3 mg mL^{-1}, 70 μL, ~4.2 mg kg^{-1}) + *hv*. The aforementioned aqueous solution was intratumorally injected into the tumor on the right side. The **TQC@PFC-1** injected mice were irradiated with 1080 nm light (0.9 W cm^{-2}, 6 min) 2 h after injections. Meanwhile, **TQC@PFC-1** injection or light irradiation alone was used as negative controls. Mouse body weight and tumor volume were monitored every two day for 15 days in total. At the end of study, all mouse major organs (heart, liver, spleen, lungs, kidneys, and tumor) were examined by hematoxylin and eosin (H & E) staining.

Author contributions

All the authors discussed the results and commented on the manuscript. J. T., Y. L. and M. W. conceived the experiments. Q. Z. and L. S. helped with the photothermal experiments. J. L., Q. Z. and X. S. helped with cell experiments. All authors have approved the manuscript.

Conflicts of interest

There are no conflicts to declare.

Acknowledgements

M. Wang acknowledges the financial support from the National Science Foundation of China (22077125 to MW) and the Beijing Natural Science Foundation (Z220023).

Notes and references

1 L. Sun, Y. Wang, F. Yang, X. Zhang and W. Hu, *Adv. Mater.*, 2019, **31**, e1902328.
2 L. Sun, W. Zhu, X. Zhang, L. Li, H. Dong and W. Hu, *J. Am. Chem. Soc.*, 2021, **143**, 19243–19256.
3 Y. Wang, H. Wu, W. Zhu, X. Zhang, Z. Liu, Y. Wu, C. Feng, Y. Dang, H. Dong, H. Fu and W. Hu, *Angew. Chem., Int. Ed.*, 2021, **60**, 6344–6350.
4 S. K. Park, S. Varghese, J. H. Kim, S. J. Yoon, O. K. Kwon, B. K. An, J. Gierschner and S. Y. Park, *J. Am. Chem. Soc.*, 2013, **135**, 4757–4764.
5 S. K. Park, J. H. Kim, T. Ohto, R. Yamada, A. O. F. Jones, D. R. Whang, I. Cho, S. Oh, S. H. Hong, J. E. Kwon, J. H. Kim, Y. Olivier, R. Fischer, R. Resel, J. Gierschner, H. Tada and S. Y. Park, *Adv. Mater.*, 2017, **29**, 1701346.
6 G. Bolla, Q. Liao, S. Amirjalayer, Z. Tu, S. Lv, J. Liu, S. Zhang, Y. Zhen, Y. Yi, X. Liu, H. Fu, H. Fuchs, H. Dong, Z. Wang and W. Hu, *Angew. Chem., Int. Ed.*, 2021, **60**, 281–289.

7 H. Li, C. Fan, W. Fu, H. L. Xin and H. Chen, *Angew. Chem., Int. Ed.*, 2015, **54**, 956–960.
8 W. Zhu, L. Zhu, L. Sun, Y. Zhen, H. Dong, Z. Wei and W. Hu, *Angew. Chem., Int. Ed.*, 2016, **55**, 14023–14027.
9 Y. Wang, H. Wu, P. Li, S. Chen, L. O. Jones, M. A. Mosquera, L. Zhang, K. Cai, H. Chen, X. Y. Chen, C. L. Stern, M. R. Wasielewski, M. A. Ratner, G. C. Schatz and J. F. Stoddart, *Nat. Commun.*, 2020, **11**, 4633.
10 S. Tian, J. Tan, T. Kang, C. Cao, J. Pan, Y. Xiao, X. Cui, S. Li and C. S. Lee, *Adv. Mater.*, 2022, **34**, e2204749.
11 M. Zhuo, Y. Yuan, Y. Su, S. Chen, Y. Chen, Z. Feng, Y. Qu, M. Li, Y. Li, B. Hu, X. Wang and L. Liao, *Adv. Mater.*, 2022, **34**, e2107169.
12 A. S. Tayi, A. K. Shveyd, A. C. Sue, J. M. Szarko, B. S. Rolczynski, D. Cao, T. J. Kennedy, A. A. Sarjeant, C. L. Stern, W. F. Paxton, W. Wu, S. K. Dey, A. C. Fahrenbach, J. R. Guest, H. Mohseni, L. X. Chen, K. L. Wang, J. F. Stoddart and S. I. Stupp, *Nature*, 2012, **488**, 485–489.
13 R. A. Wiscons, N. R. Goud, J. T. Damron and A. J. Matzger, *Angew. Chem., Int. Ed.*, 2018, **57**, 9044–9047.
14 D. Wang, X. Kan, C. Wu, Y. Gong, G. Guo, T. Liang, L. Wang, Z. Li and Y. Zhao, *Chem. Commun.*, 2020, **56**, 5223–5226.
15 W. Chen, S. Sun, G. Huang, S. Ni, L. Xu, L. Dang, D. L. Phillips and M. D. Li, *J. Phys. Chem. Lett.*, 2021, **12**, 5796–5801.
16 Y. Wang, W. Zhu, W. Du, X. Liu, X. Zhang, H. Dong and W. Hu, *Angew. Chem., Int. Ed.*, 2018, **57**, 3963–3967.
17 S. Tian, Z. Huang, J. Tan, X. Cui, Y. Xiao, Y. Wan, X. Li, Q. Zhao, S. Li and C.-S. Lee, *ACS Energy Lett.*, 2020, **5**, 2698–2705.
18 J. Xu, Q. Chen, S. Li, J. Shen, P. Keoingthong, L. Zhang, Z. Yin, X. Cai, X. Chen and W. Tan, *Angew. Chem., Int. Ed.*, 2022, **61**, e2022025.
19 W. Yin, J. Yu, F. Lv, L. Yan, L. R. Zheng, Z. Gu and Y. Zhao, *ACS Nano*, 2016, **10**, 11000–11011.
20 R. Xing, K. Liu, T. Jiao, N. Zhang, K. Ma, R. Zhang, Q. Zou, G. Ma and X. Yan, *Adv. Mater.*, 2016, **28**, 3669–3676.
21 L. Zhao, Y. Liu, R. Chang, R. Xing and X. Yan, *Adv. Funct. Mater.*, 2019, **29**, 1806877.
22 H. Xiang, Q. Yang, Y. Gao, D. Zhu, S. Pan, T. Xu and Y. Chen, *Adv. Funct. Mater.*, 2020, **30**, 1909938.
23 L. Zeng, L. Huang, Z. Wang, J. Wei, K. Huang, W. Lin, C. Duan and G. Han, *Angew. Chem., Int. Ed.*, 2021, **60**, 23569–23573.
24 Z. Ji, T. Li and O. M. Yaghi, *Science*, 2020, **369**, 674–780.
25 S. Canossa, Z. Ji, C. Gropp, Z. Rong, E. Ploetz, S. Wuttke and O. M. Yaghi, *Nat. Rev. Mater.*, 2023, **8**, 331–340.
26 S. Kandambeth, K. Dey and R. Banerjee, *J. Am. Chem. Soc.*, 2019, **141**, 1807–1822.
27 K. Sasmal, A. Mahato, P. Majumder and R. Banerjee, *J. Am. Chem. Soc.*, 2022, **144**, 11482–11498.
28 P. Li, M. R. Ryder and J. F. Stoddart, *Acc. Mater. Res.*, 2020, **1**, 77–87.
29 I. Hisaki, C. Xin, K. Takahashi and T. Nakamura, *Angew. Chem., Int. Ed.*, 2019, **58**, 11160–11170.
30 X. Song, Y. Wang, C. Wang, D. Wang, G. Zhuang, K. O. Kirlikovali, P. Li and O. K. Farha, *J. Am. Chem. Soc.*, 2022, **144**, 10663–10687.
31 B. Wang, R. B. Lin, Z. Zhang, S. Xiang and B. Chen, *J. Am. Chem. Soc.*, 2020, **142**, 14399–14416.
32 R. B. Lin, Y. He, P. Li, H. Wang, W. Zhou and B. Chen, *Chem. Soc. Rev.*, 2019, **48**, 1362–1389.
33 J. Yang, J. Wang, B. Hou, X. Huang, T. Wang, Y. Bao and H. Hao, *Chem.Eng. J.*, 2020, **399**, 125873.
34 M. Vicent-Morales, M. Esteve-Rochina, J. Calbo, E. Orti, I. J. Vitorica-Yrezabal and G. Minguez Espallargas, *J. Am. Chem. Soc.*, 2022, **144**, 9074–9082.
35 A. Zhang, D. Si, H. Huang, L. Xie, Z. B. Fang, T. F. Liu and R. Cao, *Angew. Chem., Int. Ed.*, 2022, **61**, e202203955.
36 Y. Sun, J. Wei, Z. Fu, M. Zhang, S. Zhao, G. Xu, C. Li, J. Zhang and T. Zhou, *Adv. Mater.*, 2022, e2208625.
37 X. Ding, Z. Liu, Y. Zhang, G. Ye, J. Jia and J. Chen, *Angew. Chem., Int. Ed.*, 2022, **61**, e202116483.
38 Q. Yin, P. Zhao, R. J. Sa, G. C. Chen, J. Lü, T. F. Liu and R. Cao, *Angew. Chem., Int. Ed.*, 2018, **57**, 7691–7696.
39 B. T. Liu, X. H. Pan, D. Y. Nie, X. J. Hu, E. P. Liu and T. F. Liu, *Adv. Mater.*, 2020, **32**, e2005912.
40 B. T. Liu, X. H. Pan, D. Y. Zhang, R. Wang, J. Y. Chen, H. R. Fang and T. F. Liu, *Angew. Chem., Int. Ed.*, 2021, **60**, 25701–25707.
41 W. Liang, F. Carraro, M. B. Solomon, S. G. Bell, H. Amenitsch, C. J. Sumby, N. G. White, P. Falcaro and C. J. Doonan, *J. Am. Chem. Soc.*, 2019, **141**, 14298–14305.
42 G. Chen, S. Huang, Y. Shen, X. Kou, X. Ma, S. Huang, Q. Tong, K. Ma, W. Chen, P. Wang, J. Shen, F. Zhu and G. Ouyang, *Chem*, 2021, **7**, 2722–2742.
43 G. Chen, L. Tong, S. Huang, S. Huang, F. Zhu and G. Ouyang, *Nat. Commun.*, 2022, **13**, 4816.
44 Z. Tang, X. Li, L. Tong, H. Yang, J. Wu, X. Zhang, T. Song, S. Huang, F. Zhu, G. Chen and G. Ouyang, *Angew. Chem., Int. Ed.*, 2021, **60**, 23608–23613.
45 P. Wied, F. Carraro, J. M. Bolivar, C. J. Doonan, P. Falcaro and B. Nidetzky, *Angew. Chem., Int. Ed.*, 2022, **61**, e202117345.
46 J. Tang, J. Liu, Q. Zheng, W. Li, J. Sheng, L. Mao and M. Wang, *Angew. Chem., Int. Ed.*, 2021, **60**, 22315–22321.
47 D. Yu, H. Zhang, Z. Liu, C. Liu, X. Du, J. Ren and X. Qu, *Angew. Chem., Int. Ed.*, 2022, **61**, e202201485.
48 H. Zhang, D. Yu, S. Liu, C. Liu, Z. Liu, J. Ren and X. Qu, *Angew. Chem., Int. Ed.*, 2022, **61**, e202109068.
49 D. K. Roper, W. Ahn and M. Hoepfner, *J. Phys. Chem. C*, 2007, **111**, 3636–3641.

